

# Hybrid regularization for MRI reconstruction with static field inhomogeneity correction

Ryan Compton<sup>\* \*1</sup>, Stanley Osher<sup>1</sup>, and Louis-S. Bouchard<sup>2</sup>

<sup>1</sup>Department of Mathematics, University of California, Los Angeles, CA 90095, USA.

<sup>2</sup>Department of Chemistry, University of California, Los Angeles, CA, 90095, USA.

January 6, 2013

## Abstract

Rapid acquisition of magnetic resonance (MR) images via reconstruction from undersampled  $k$ -space data has the potential to greatly decrease MRI scan time on existing medical hardware. To this end, iterative image reconstruction based on the technique of compressed sensing has become the method choice for many researchers [1]. However, while conventional compressed sensing relies on random measurements from a discrete Fourier transform, actual MR scans often suffer from off-resonance effects and thus generate data by way of a non-Fourier operator [2]. Correcting for these effects requires that one employs more sophisticated image reconstruction methods and introduces computational bottlenecks that are not encountered in standard compressed sensing.

In this work, we demonstrate how one may accelerate the convergence of algorithms for solving the image reconstruction problem,

$$\underset{\rho}{\operatorname{argmin}} J(\rho) \text{ subject to } A\rho = s \quad (1)$$

by opting for a regularization of the form:

$$J(\rho) = |\nabla\rho| + \nu|F\rho| \quad (2)$$

when  $F$  is a tight frame and  $A$  is only approximately a Fourier transform. In our experiments, reconstructing field-corrected MR images with the hybrid regularization of eq. (2) provides a speedup of roughly one order of magnitude when compared with an approach based solely on total-variation and may produce higher quality images than an approach based solely on tight frames.

## 1 Introduction

While the problem of image reconstruction in magnetic resonance imaging (MRI) has a long history, the techniques employed usually assume the static magnetic field is homogeneous and the applied magnetic-field gradients are unidirectional with constant magnitude [3]. In recent years, the prospects of generating MRI images using portable sensors have been explored [4] [5]. Although some efforts have focused on generating remote homogeneous fields [6], most portable sensors are

---

<sup>\*</sup>rcompton@math.ucla.edu

single-sided and characterized by inhomogeneous fields [7] [8]. The inhomogeneous field can be used to select a slice for imaging [4]. In other instances, so-called “shimming” radio-frequency (RF) pulses have been used to prepare the spins and impart a phase that compensates for the effects of an inhomogeneous field [9] [10] [11]. In the limit of low magnetic fields, the magnetic-field gradients are no longer unidirectional according to Maxwell’s equations in the absence of a rotating-wave approximation. MRI is still feasible with the use of coherent averaging techniques [12] [13], oscillating fields [14] or spatial shimming [15]. Each of these techniques have limitations. For coherent averaging and RF shimming techniques, the stroboscopic sequences required are not practical for *in vivo* use because of RF heating and the short  $T_2$  relaxation times in tissues. In this article, we treat the problem of image reconstruction in high-field MRI, in the presence of inhomogeneous static and gradient magnetic fields. The direct reconstruction (as opposed to the use of compensating techniques) may be the preferred approach in clinical applications, where rapid imaging is required.

The most general MRI reconstruction problem assumes no rotating-wave approximation. Spins precess about a field  $\vec{B}(\mathbf{x}, t)$  which may include time-dependent gradients. Its direction and magnitude may be a function of space. Because of the time-dependence of the local field, the rotations are non-commutative and a time-ordered product must be used to describe its effect. For spin  $I = 1/2$ , the rotations are described by the spin operators  $I_i = \sigma_i/2$ ,  $i = x, y, z$ , where  $\sigma_i$  are the Pauli matrices. The rotation operator is written in terms of Dyson time-ordering  $\vec{T}$ :

$$U(\mathbf{x}, t) = \vec{T} e^{i\gamma \int_0^t [I_x B_x(\mathbf{x}, t) + I_y B_y(\mathbf{x}, t) + I_z B_z(\mathbf{x}, t)] dt}$$

The initial state of the nuclear magnetization density can be expressed as  $\rho(\mathbf{x}) = I_x \rho_x(\mathbf{x}) + I_y \rho_y(\mathbf{x}) + I_z \rho_z(\mathbf{x})$ . It is evolved in time according to the unitary transformation  $\rho(\mathbf{x}, T) = U^\dagger(\mathbf{x}, T) \rho(\mathbf{x}) U(\mathbf{x}, T)$ . Detection is done along a given axis defined by a field  $\vec{B}_1(\mathbf{x})$ . Neglecting relaxation effects, the NMR signal is therefore proportional to the volume integral of the Hilbert space trace (Tr):

$$s(t) = \int_V \text{Tr}[\{B_{1x}(\mathbf{x})I_x + B_{1y}(\mathbf{x})I_y + B_{1z}(\mathbf{x})I_z\} U^\dagger(\mathbf{x}, t) \rho(\mathbf{x}) U(\mathbf{x}, t)] d^3\mathbf{x}. \quad (3)$$

The image reconstruction problem consists of solving for the magnetization distribution  $\rho(\mathbf{x})$  by measuring  $s(t)$  at different times  $t$  while time-modulating the gradients.

If a strong static magnetic field is applied, only the components of the magnetic field gradients parallel to the static magnetic field are preserved. The perpendicular components of the gradient fields rapidly average to zero. This rotating-wave approximation leads to a local magnetic field whose direction remains fixed. Only its magnitude can change with time. Therefore, time-ordered rotations are no longer needed. The signal equation reduces to a simpler expression:

$$s(t) = \int_V \rho(\mathbf{x}) e^{-z(\mathbf{x})t} e^{-2\pi i \mathbf{k}(t) \cdot \mathbf{x}} d\mathbf{x} \quad (4)$$

where  $s(t_i)$  is the recorded signal,  $z(\mathbf{x})$  describes the off-resonance effects (imaginary part). Relaxation effects can be included in  $z(\mathbf{x})$  (real part). The magnetization density,  $\rho(\mathbf{x})$ , is a scalar-valued field. The goal of MRI reconstruction is to solve for the proton density map,  $\rho(\mathbf{x})$ , in the signal equation. The  $k$ -space coordinates,  $\mathbf{k}(t)$ , which are defined by the applied gradients, are known only on a nonuniform and possibly undersampled grid [16]. The gradients are assumed to be uniform. For a 2D slice,  $V$  is a subset of  $\mathbb{R}^2$ .

A  $n$ -point discretization of the physical space integral at  $m$  different values of  $t$  leads to the  $m \times n$  linear system

$$s = A\rho \quad (5)$$

with system matrix

$$A_{ij} = e^{-z(\mathbf{x}_j)t_i} e^{-2\pi i \mathbf{k}(t_i) \cdot \mathbf{x}_j}. \quad (6)$$

Efficiently inverting the linear system (5) in a way that produces high quality images is central to MRI.

With conventional MRI methods the background field is assumed perfectly homogeneous and the phase accrual due to off resonant frequency,  $e^{-z(\mathbf{x}_j)t_i}$ , is then ignored. Here,  $A$  becomes a Fourier encoding matrix and image reconstruction may be accomplished by directly inverting  $A$  or, in the event that our system is underdetermined, solving a regularized inverse problem using methods from compressed sensing [17]. Regularization terms based on total variation [1], wavelets [18], and shearlets [19] have been successful. In the more general case of parallel imaging these regularizations still provide quality images [20].

While simple computationally, failing to accommodate for off-resonance effects often leads to blurring and image distortion in many types of MR scans. These effects are often due to abrupt spatial variations in the magnetic susceptibility of biological tissues being imaged. Near interfaces between regions of different susceptibility, the static background field,  $B_0$ , is perturbed by an additional, weaker, magnetic field,  $\Delta B(\mathbf{x})$ , whose strength is proportional to the strength of the background field and a function depending on the tissue, i.e.  $\Delta B(\mathbf{x}) = \chi_m(\mathbf{x})B_0$  [21]. The final background field,  $B_0 + \Delta B(\mathbf{x})$ , thus varies in space.

The value of  $\chi_m$  is often small (for grey matter,  $\chi_m \approx 8.97 \times 10^{-6}$  [21]). However, new developments in MRI technology are leading to stronger  $B_0$  fields where the off-resonance effects are more substantial [22]. In ultra-high field MRI (i.e.  $\geq 7$  T), static field inhomogeneities place notable limitations on the images a device can produce [22].

Standard examples of images corrupted by off-resonance effects are found in cranial MRI scans near air/tissue interfaces. Here, the differences in magnetic susceptibility between air and water are responsible for the creation of the perturbing field [23]. The situation occurs again when imaging regions containing gray/white matter boundaries [21]. As a result, correcting for off-resonance effects is of specific importance for surgical planning near the nasal sinuses, auditory canals, and cerebral cortex [24] [25].

Nonstandard examples occur when imaging patients who use hair products containing iron oxide or cobalt particles [26]. Proper maintenance of “twists” or “dreadlocks” mandates that hair is saturated with beeswax (or colored beeswax) near the scalp in order to prevent essential knots from coming undone. Magnetization of the hair product leads to strong static field inhomogeneities and thus highly distorted images. A similar effect occurs when scanning patients wearing colored eye makeup [27].

To compensate for these distortions, we first note that the off-resonance factor,  $e^{-z(\mathbf{x})t}$ , in the image model eq. (4) is multiplied with the proton density map in  $k$ -space. This leads to a convolution in physical space. The reconstruction problem thus involves deconvolution in addition to Fourier decoding.

We focus on the case where  $e^{-z(\mathbf{x})t}$  is known beforehand (i.e. non-blind deconvolution). There is a large and growing body of work aimed at determining  $z(\mathbf{x})$ . Current methods make use of many ideas that overlap with techniques used in general image processing. Some examples include determination of a field map via MAP estimation [28] as well as  $l_1$ -penalized optimization [29].

Knowing the field map, however, does not immediately provide one with a prescription for high quality image formation as the matrix

$$E_{ij} = e^{-z(\mathbf{x}_j)t_i} \quad (7)$$

is often so large that storage is impossible on most modern desktops [30]. As an example, to produce a  $512 \times 512$  image the (dense)  $E$  matrix takes on dimensions  $512^2 \times 512^2$ . Storing  $E$  in 32-bit floating point precision requires 256GB of space. Consequently, directly forming the system matrix,  $A$ , is infeasible for practical image sizes and some form of operator compression must be employed in the reconstruction procedure [31] [32].

Once a procedure to apply  $E$  is known and  $k$ -space has been fully sampled one may reconstruct  $\rho$  using a variety of techniques [33] [34] [35]. Non-iterative approaches for field correction, such as the conjugate phase methods of [36], [37] and [38] are fast and commonly used. However, in recent years, iterative approaches based on regularization have come into favor as they ignore this assumption and produce higher quality images. The drawback to iterative methods tends to be an increase in computational cost [31].

One unexpected advantage of iterative reconstruction methods is the almost exact overlap they have with the recent and prolific theory of compressed sensing. As a result, recent years have seen tremendous progress in fast algorithms for iterative reconstruction [39]. The canonical problem in both methods is:

$$\underset{\rho}{\operatorname{argmin}} J(\rho) \text{ subject to } A\rho = s \quad (8)$$

where  $J$  represents some form of sparsity promoting regularization.

Traditional iterative image reconstruction methods are known to be very reliable when a large amount of  $k$ -space has been acquired [32]. In the absence of off-resonance effects, it is known from compressed sensing that exact image reconstruction is possible from extremely undersampled  $k$ -space data [17].

In this work, we propose solutions when these two issues are combined, providing a method for image recovery with a generalized operator when  $k$ -space is undersampled. Furthermore, we introduce a regularization term based on framelets [40] and establish a significant reduction in computational cost when this term is included.

## 2 Method

### 2.1 Low-rank inhomogeneity correction

Before we can successfully carry out any iterative solution procedure we must first be able to apply our system matrix. Writing  $A$  as the pointwise matrix product,

$$A = E \circ \mathcal{F} \quad (9)$$

we can see that a low-storage approximation to  $E$  will yield an approximation to  $A$  which fits in memory as the Fourier operator requires no storage.

Given a target rank,  $r$ , we construct a low-rank approximation to the off-resonance matrix,

$$E \approx BC \quad (10)$$

where  $B \in \mathbb{R}^{m \times r}$  and  $C \in \mathbb{R}^{r \times n}$  are thin. Now,

$$s_i = \sum_{j=1}^n A_{ij} \rho_j \quad (11)$$

$$= \sum_{j=1}^m E_{ij} \circ \mathcal{F}_{ij} \rho_j \quad (12)$$

$$\approx \sum_{j=1}^m \sum_{l=1}^r B_{il} C_{lj} \mathcal{F}_{ij} \rho_j \quad (13)$$

$$= \sum_{l=1}^r \sum_{j=1}^m B_{il} C_{lj} \mathcal{F}_{ij} \rho_j \quad (14)$$

$$= \sum_{l=1}^r B_{il} \sum_{j=1}^m \mathcal{F}_{ij} C_{lj} \rho_j \quad (15)$$

leading to,

$$A \approx \sum_{l=1}^r \text{diag}(B_{(:,l)}) \mathcal{F} \text{diag}(C_{(l,:)}) \quad (16)$$

where  $\text{diag}(B_{(:,l)})$  and  $\text{diag}(C_{(l,:)})$  are diagonal matrices with entries taken from the  $l$ th column and row of  $B$  and  $C$ , respectively. Provided that the singular values of  $E$  decay quickly enough that the low-rank approximation eq. (10) is valid, we may rapidly apply  $A$  with little storage overhead using eq. (16). It turns out that this is indeed the case for empirically observed field maps [41]. As the inhomogeneities become stronger, higher rank approximations are needed to accurately describe  $E$ .

When working with nonuniformly or undersampled  $k$ -space data we only need to replace the Fourier matrix with a discrete nonuniform Fourier transform operator (NUFFT) of type 2 [42]. In which case we write

$$A \approx \sum_{l=1}^r B_l \mathcal{G} C_l. \quad (17)$$

## 2.2 Forming the approximation

For the matrix decomposition,  $E \approx BC$ , several methods can be found in recent literature on MRI reconstruction [41] [43] [44] [45] [46]. The common foundation on which all these methods are built is approximation of the exponential,

$$e^{-z(\mathbf{x}_j)t_i} \approx \sum_{l=1}^r B_{il} C_{lj}. \quad (18)$$

Strategies for forming eq. (18) can be split into roughly two camps: those that focus on functional approximations of the form

$$e^{-z(\mathbf{x})t} = \sum_{l=1}^r b_l(t) c_l(\mathbf{x}) \quad (19)$$

and those that treat the decomposition as a general low-rank matrix approximation problem.

Matrix-based approaches typically lead to the most accurate approximations for a given rank, but require substantial computational overhead as the matrix,  $E$ , must be examined in full. Recent developments in randomized algorithms originating within the numerical linear algebra community may somewhat alleviate this burden [47] [48] [49].

### 2.2.1 Interpolative Decompositions

For a purely algebraic approach to the decomposition, we introduce a recently developed matrix factorization [50]:

**Definition 1** (Interpolative Decomposition). *Let  $E \in \mathbb{R}^{n \times n}$  have rank at most  $r$ . The decomposition*

$$E_{n \times n} = B_{m \times r} C_{r \times n} \quad (20)$$

*where the columns of  $B$  make up a subset of the columns of  $E$ , and each entry in  $C$  had magnitude at most two, is referred to as the interpolative decomposition of  $E$ .*

Thus, we form an approximation to  $E$  using a bounded linear combination of a few columns of  $E$ . The existence of an interpolative decomposition for  $|C_{ij}| \leq 1$  is established in [51]. Computation of such a  $C$ , however, turns out to be *NP*-hard [52].

Computing an interpolative decomposition is fairly straightforward when a capable linear algebra library is available. Difficulties may arise when one does not have access to a pivoted-*QR* decomposition or any linear system solvers.

---

**Algorithm 1:** Interpolative Decomposition for low-rank  $E$ .

---

Form  $Q_{n \times r} R_{r \times n} \Pi_{n \times n} = E_{n \times n}$  via a pivoted-*QR* decomposition [53]

Define  $S_{r \times r}$  and  $T_{r \times (n-r)}$  by  $(S_{r \times r} \mid T_{r \times (n-r)}) = R_{r \times n}$

Compute  $B_{n \times r} = Q_{n \times r} S_{r \times r}$

Compute  $C_{r \times n} = (1_{r \times r} \mid (S^{-1})_{r \times r} T_{r \times (n-r)}) \Pi_{n \times n}$

---

The columns of  $B$  are a subset of the columns of  $E$  since they are determined by multiplying  $Q$  with columns of the  $R$  matrix found in the *QR* decomposition of  $E$ . The matrix  $S$  is small in our applications (e.g.  $S \in \mathbb{R}^{10 \times 10}$ ) so that the inversion is easily computed.

The decomposition in algorithm 1 is exact when the rank of  $E$  is exactly  $r$ . In the general setting, where  $E$  is high-rank and we seek a low-rank approximation, we have the estimate for each  $r$ :

$$\|E_{n \times n} - B_{n \times r} C_{r \times n}\| \lesssim \sigma_{r+1} \quad (21)$$

where  $\sigma_{r+1}$  is the  $r + 1$ st greatest singular value of  $E$  [54].

For matrix compression tasks, we premultiply  $E$  with a Gaussian random matrix,  $G \in \mathbb{R}^{r \times m}$ , before factoring [50]. Applying  $E$  to a small random matrix allows us to work in a reduced subspace which approximates the range of  $E$ . Only one read of  $E$  is needed to form the product. When a few buffer vectors are added to  $G$  (leading to  $G \in \mathbb{R}^{p \times m}$  with  $p \geq r$ ) the accuracy of this approximation is notably improved. Sharp bounds on the error eq. (21) are a topic of current research [49].

---

**Algorithm 2:** Randomized Interpolative Decomposition for rank- $r$  approximation to  $E$ .

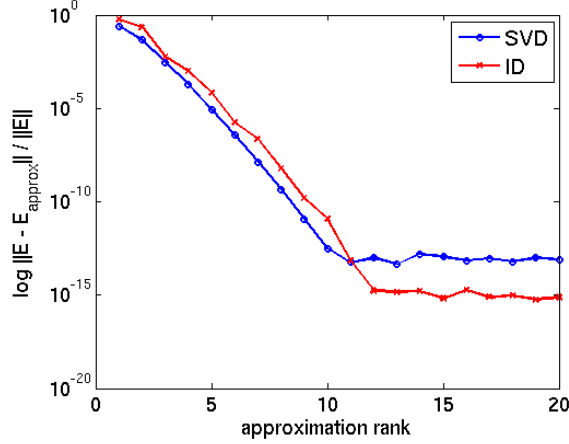
---

Compute  $Y_{p \times n} = G_{p \times n} E_{n \times n}$  for an integer  $p \geq r$

Form  $Z_{p \times r} C_{r \times n} \approx Y_{r \times n}$  using algorithm 1

The columns of  $Z$  correspond to columns of  $Y$ . That is, for  $j = 1 \dots l$  we can find  $i_1 \dots i_l$  such that the  $j$ th column of  $Z$  is the  $i_j$ th column of  $Y$ . Form  $B_{m \times r}$  by selecting columns  $i_1 \dots i_r$  from  $E_{m \times n}$ .

---



**Figure 1:** Relative error,  $\log \left( \frac{\|E - E_{approx}\|}{\|E\|} \right)$ , for varying rank approximations using a partial SVD (blue) and randomized interpolative decompositions (red). The field map is  $64 \times 64$  leading to a  $4096 \times 4096$   $E$  matrix. Machine precision is  $10^{-15}$ . High accuracy approximations at low rank are possible with a single pass over the data.

### 2.2.2 Functional decompositions

An alternative way to form the approximation eq. (10) is by explicitly approximation the exponential in the form of eq. (19). Standard approaches begin by selecting a subset of points uniformly from either the time or “frequency” domain [44].

Segmenting in the time domain is accomplished by first choosing a set of points  $\{\tilde{t}_l\}_{l=1}^r$  and a single value,  $\bar{z}$ , to approximate the field map. One then has the formulas

$$B_{il} = b_l(t_i)e^{-\bar{z}t_i} \quad (22)$$

$$C_{lj} = e^{-(z(\mathbf{x}_j) - \bar{z})\tilde{t}_l}. \quad (23)$$

Interpolating functions,  $b_l(t)$ , are used to evaluate the coefficients between each pair of  $\tilde{t}_l$ . The method used to interpolate the time domain has a large effect on the accuracy of this approach. Current methods favor a “min-max” approach [32].

Selecting  $\bar{z} = 0$  corresponds to standard unidirectional interpolation of the function  $e^{-z(\mathbf{x})t}$ . Choosing an optimal  $\bar{z}$  improves accuracy when the  $\tilde{t}_l$  are fixed in advance, optimizing the  $\tilde{t}_l$  can lead to situations where the choice of  $\bar{z}$  is irrelevant [30]. A comparison of many currently available methods for approximations of the form eq. (19) can be found in [41].

### 2.3 Restricted isometry constraints

A difficulty with the corrected system arises when we attempt to make the extreme reductions in  $k$ -space data that were suggested in the original compressed sensing literature. The modified system matrix obeys uncertainty properties differing from the pure Fourier case and no longer have the same guarantees on exact signal reconstruction [55].

Recall the concept of a *restricted isometry constant*,  $\delta_s^A$ , of a matrix  $A$  for an integer  $s$  as the smallest number such that

$$(1 - \delta_s^A)\|x\|_{l_2}^2 \leq \|Ax\|_{l_2}^2 \leq (1 + \delta_s^A)\|x\|_{l_2}^2 \quad (24)$$

where  $s$  is the number of nonzero entries in  $x$ . When such a constant exists  $A$  is said to satisfy the *restricted isometry property*. This property guarantees exact image reconstruction from vastly undersampled  $k$ -space with overwhelmingly high probability. In the case of an undersampled Fourier matrix, much work has been devoted to showing that  $\delta_s^{\mathcal{G}}$  is small [56].

In our corrected system, we can infer that each term in the sum eq. (18) has less than ideal isometric properties by examining

$$\|B_l \mathcal{G} C_l x\|_2 \leq \|B_l\| \|\mathcal{G} C_l x\|_2 \quad (25)$$

$$\leq \max_i(b_{il})(1 + \delta_s^{\mathcal{G}}) \max_j(c_{lj}) \|x\|_2 \quad (26)$$

By combining eq. (26) with the analogous lower bound a crude estimate for the restricted isometry constant for an  $r = 1$  correction to our inhomogeneity can be found

$$\delta_s^{B_l \mathcal{G} C_l} \leq \min \left( 1 - \min_i(b_{il}) \min_j(c_{lj}) + \min_i(b_{il}) \min_j(c_{lj}) \delta_s^{\mathcal{G}}, 1 - \max_i(b_{il}) \max_j(c_{lj}) \delta_s^{\mathcal{G}} + \max_i(b_{il}) \max_j(c_{lj}) \delta_s^{\mathcal{G}} \right). \quad (27)$$

Larger values of  $r$  increase the corresponding isometry constants and as a result more samples are required for accurate image recovery than in the pure Fourier case. Smaller values of  $r$  result in poorer approximations to the correction matrix. In this work, we choose  $r$  such that  $E$  is well approximated and accept that more  $k$ -space samples must be acquired.

While the restricted isometry constant is independent of the reconstruction technique, the fact that our problem has suboptimal isometric properties has influenced our choice of regularization. Framelets, like wavelets, give high-quality image decompositions using a multiscale basis. However, unlike wavelets, framelet bases are redundant and allow more accurate image representations than possible with orthogonal wavelet bases. These particular redundant basis elements have high order vanishing moments, which should explain the accuracy, even near discontinuities [57]. Total variation is well-known for its ability to remove noise and preserve edges [58]. We compensate for a poor restricted isometry constant by incorporating substantial information about image structure into our regularization.

## 2.4 Sparse recovery via $l1$ minimization

We propose a reduction in scan time by appealing to the theory of compressed sensing, downsampling our Fourier matrix uniformly at random and accounting for the missing data with sparsity promoting regularization.

While MR images are not sparse in the image domain, they are sparse in an appropriately chosen transform domain [1]. Representation of images in bases of wavelets, and by extension, framelets yield sparse collections of coefficients [40]. Similarly, reconstruction methods based on the total variation norm well as its nonlocal counterpart have been shown to accurately reproduce detailed images from sparse frequency data [59].

We advocate a composite of total variation and framelet regularization,

$$J(\rho) = |\nabla \rho| + \nu |F \rho| \quad (28)$$

where the first term is a total variation norm and  $F$  is the discrete framelet decomposition [40]. The total variation term enhances edges in our reconstructed image while the inclusion of the framelet



term allows us to reconstruct smooth images. The parameter  $\nu$  is chosen by the user and controls the relative importance of edges versus smoothness in the sought after image.

It has been found previously that hybrid regularization based on wavelets often improves image quality [39]. Our framelet based regularization extends this work to redundant orthogonal bases where natural images can be represented more accurately.

## 2.5 Split Bregman iterations for image recovery

Our image is the solution to the constrained optimization eq. (1) which we solve with the Split Bregman method of [39]. We begin by converting the constrained optimization into a sequence of unconstrained problems via Bregman iteration:

$$\begin{cases} \rho^{k+1} &= \min_{\rho} |\nabla \rho| + \nu |F\rho| + \frac{\mu}{2} \|A\rho - s^k\|^2 \\ s^{k+1} &= s^k + s - A\rho^{k+1} \end{cases} \quad (29)$$

where the parameter  $\mu$  affects the convergence rate and is chosen by the user [60]. Typical values of  $\mu$  range between 0.5 and 1. High values of  $\mu$  better enforce the constraint at each iteration but have the drawback that the  $\rho^{k+1}$  update becomes harder to solve [39]. Alternately updating  $\rho^k$  and  $s^k$  produces a sequence,  $\rho^k$ , known to converge to the solution of the constrained optimization problem,  $\rho$  [61].

Updating  $s^k$  is straightforward. Minimization of the unconstrained step in eq. (29) is done by introducing auxiliary variables,  $d_x = \nabla_x \rho$ ,  $d_y = \nabla_y \rho$ , and  $w = F\rho$ , allowing us to rewrite our  $\rho^k$  update in the equivalent split form

$$\rho^{k+1} = \min_{\rho} |\nabla d| + \nu |w| + \frac{\mu}{2} \|A\rho - s^k\|^2 \quad (30)$$

$$\text{subject to } \begin{cases} (d_x, d_y) = (\nabla_x \rho, \nabla_y \rho) \\ w = F\rho \end{cases} \quad (31)$$

This constrained optimization is then converted to a sequence of unconstrained problems via a second Bregman iteration leading us to the following algorithm:

---

**Algorithm 3:** Split Bregman iteration for constrained optimization

---

**Initialize:**  $\rho^0 = A^t s$ , and  $d_x^0 = d_y^0 = w^0 = b_x^0 = b_y^0 = b_w^0 = 0$

**while**  $\|A\rho^k - s\|_2^2 > \text{tol}$  **do**

**for**  $i = 1$  **to**  $n_{\text{inner}}$  **do**

$$\rho^{k+1} = \min_{\rho} \frac{\mu}{2} \|A\rho - s^k\|^2 + \frac{\lambda}{2} \|d_x^k - \nabla_x \rho - b_x^k\|^2 + \frac{\lambda}{2} \|d_y^k - \nabla_y \rho - b_y^k\|^2 + \frac{\gamma}{2} \|w^k - F\rho - b_w^k\|^2$$

$$d_x^{k+1} = \text{shrink}(\nabla_x \rho^{k+1} + b_x^k, 1/\lambda)$$

$$d_y^{k+1} = \text{shrink}(\nabla_y \rho^{k+1} + b_y^k, 1/\lambda)$$

$$w^{k+1} = \text{shrink}(F\rho^{k+1} + b_w^k, \nu/\gamma)$$

$$b_x^{k+1} = b_x^k + (\nabla_x \rho^{k+1} - d_x^{k+1})$$

$$b_y^{k+1} = b_y^k + (\nabla_y \rho^{k+1} - d_y^{k+1})$$

$$b_w^{k+1} = b_w^k + (F\rho^{k+1} - w^{k+1})$$

**end**

$$s^{k+1} = s^k + s - A\rho^{k+1}$$

**end**

---

Here, the function *shrink* comes from the wavelet literature and is defined as

$$\text{shrink}(\xi, a) = \frac{\xi}{|\xi|} \max(|\xi| - a, 0). \quad (32)$$

The constants  $\lambda$  and  $\gamma$  are chosen by the user and affect the convergence rate.

Computationally, the  $\rho^{k+1}$  update is the most expensive part of our algorithm by a wide margin. The speed of our image reconstruction is determined by how fast we can solve this minimization. In the purely Fourier case, an analytic solution exists leading to a notably fast algorithm [39]. We have no such formula for the generalized  $A$  we work with and instead rely on iterations of the conjugate gradient method to update  $\rho^{k+1}$ .

By differentiating with respect to  $\rho$  and setting the result to zero we find our  $\rho^{k+1}$  update as the solution to:

$$(\mu A^t A + \lambda \nabla_x^t \nabla_x + \lambda + \gamma F^t F) \rho^{k+1} = r h s^k \quad (33)$$

where

$$r h s^k = \mu A^t s^k + \lambda \nabla_x^t (d_x^k - b_x) + \lambda \nabla_y^t (w - b_w). \quad (34)$$

Making use of the identities  $\nabla^t \nabla = -\Delta$  and  $F^t F = I$ , gives the system

$$(\mu A^t A - \lambda \Delta + \gamma I) \rho^{k+1} = r h s^k \quad (35)$$

which we solve with conjugate gradient iterations.

A major advantage of our hybrid regularizer is now apparent. Consider the system resulting from a regularization based only on total variation (ie  $\gamma = 0$ ),

$$(\mu A^t A - \lambda \Delta) \rho^{k+1} = r h s^k. \quad (36)$$

Denoting maximal and minimal eigenvalues of the matrix in eq. (36) by  $\lambda_{\max}$  and  $\lambda_{\min}$  we can write the condition number of our hybrid regularized system as

$$\frac{\lambda_{\max} + \gamma}{\lambda_{\min} + \gamma} < \frac{\lambda_{\max}}{\lambda_{\min}} \quad (37)$$

notably speeding our updates.

## 2.6 Remarks on convergence

The convergence of algorithm 3 has been established in [62]. There, an equivalence between the Split-Bregman algorithm and the alternating direction method of multipliers (ADMM) is established allowing us to guarantee convergence of algorithm 3 by appealing to the vast literature on convergence results for ADMM [63].

The convergence rate for ADMM is known to be linear [64] while the conjugate-gradient method used in our updates converges superlinearly [65]. While altering the parameters in our regularization (i.e. increase  $\gamma$ ) could potentially slow the convergence of ADMM, the superlinear benefit we get from a faster-converging conjugate-gradient iteration more than makes up for this.

Due to our low-rank inhomogeneity correction, the image reconstruction problem we are solve is only an approximation to our physical model of MR signal acquisition. For a given rank,  $r$ , denote the rank- $r$  approximate image reconstruction problem by

$$P_r(\rho) = \min_{\rho} |\nabla \rho| + \nu |F \rho| + \frac{\mu}{2} \|A_r \rho - s^k\|^2 \quad (38)$$

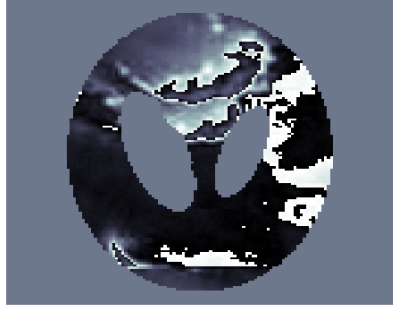
With the exact image reconstruction problem as

$$P(\rho) = \min_{\rho} |\nabla \rho| + \nu |F \rho| + \frac{\mu}{2} \|A \rho - s^k\|^2 \quad (39)$$

It is not clear that  $P_r(\rho) \rightarrow P(\rho)$ , however, work has been done in [57] establishing that this is indeed the case. Empirical evidence from the biomedical engineering community as well as the simulations in section 3 further justify the use of our matrix approximation [30] [31] [32].



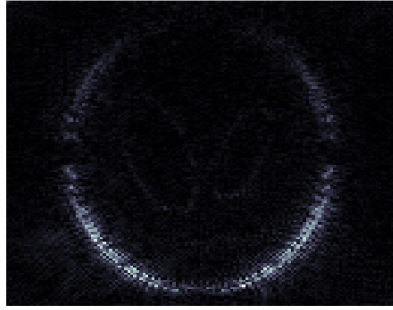
(a) 128x128 Shepp-Logan phantom



(b) Simulated field map,  $z(\mathbf{x})$  (values range between  $-15$  and  $15$  Hz)



(c) Phantom reconstruction without field map correction



(d) Magnitude of difference between fig. 2a and fig. 2c

**Figure 2:** Phantom and simulated field map data used in experiments.

### 3 Numerical Results

Our hybrid reconstruction method is compared against three alternate approaches: uncorrected nonuniform-FFT, field corrected total variation regularization, and field corrected framelet regularization.

The nonuniform Fourier transforms are computed with the min-max method of [30] using 6 points of interpolation. Piecewise linear B-spline framelets [40] are the framelet of choice. An open source implementation of the framelet transformation is available at <http://www.math.ucla.edu/~jegilles/BregmanCookbook.html>.

The majority of our computation time is spent in the FFT as each application of  $A$  requires only FFTs and diagonal matrix multiplication. High quality, scalable, parallel FFT implementations are readily available [66] and our algorithm thus adapts naturally to parallel architectures.

Numerical experiments were run in 64-bit Matlab on twelve cores of a dual hex core system compromised of two 2.67 GHz Intel Xeon CPUs with 12 MB of level 2 cache each and 50 GB of RAM.

In every image reconstruction experiment we fixed  $\mu = 0.5$ . When a total variation term was present we set  $\lambda = 0.5$ . When a framelet term was present we set  $\gamma = 5.0$ . The rank of the low-rank approximation to  $E$  is fixed at 10 and computed using a randomized interpolative decomposition.

In our three-dimensional experiment we set  $\mu = 1$ ,  $\lambda = 0.5$ , and  $\gamma = 5.0$ . We approximated  $E$  with rank a 6 approximation computed using time interpolation.



(a) TV



(b) Framelet

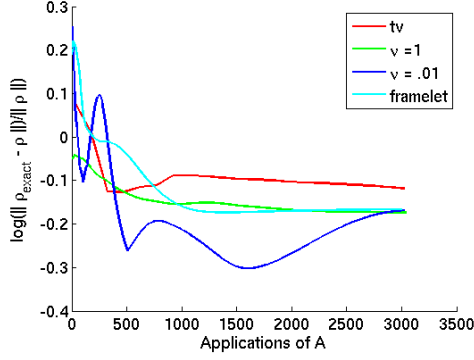


(c) Hybrid,  $\nu = 1$

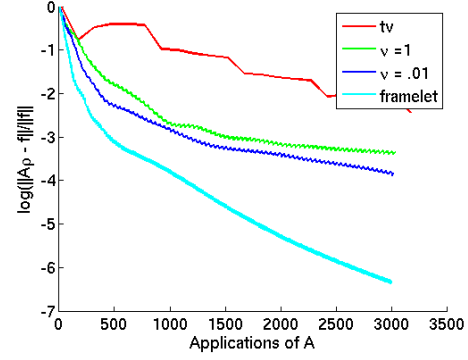


(d) Hybrid,  $\nu = .01$

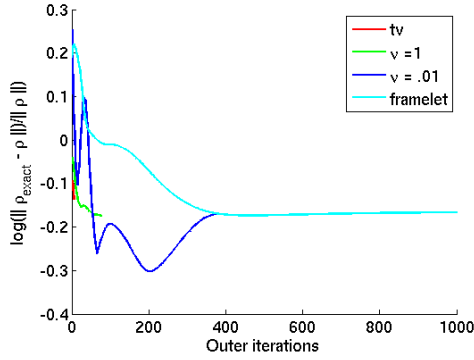
**Figure 3:** Comparison of phantom reconstructions from 20% data. All experiments were stopped after 3000 applications of  $A$ , independent of convergence. Average computation time was 88.35 seconds. The phantom is exactly piecewise constant and thus amenable to total variation regularization. However, the poor conditioning of eq. (36) prevents us from reaching the desired image in time. The highest quality image is fig. 3d, likely due to the facts that total variation is a good fit for the phantom and the positive  $\nu$  allows us to optimize fast.



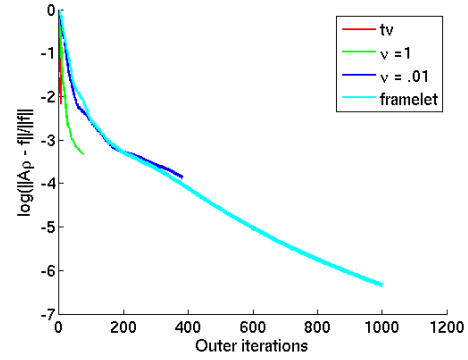
(a) Image domain errors per application of  $A$



(b) Residual errors per application of  $A$

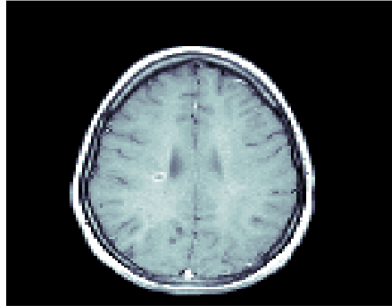


(c) Image domain errors per outer iteration

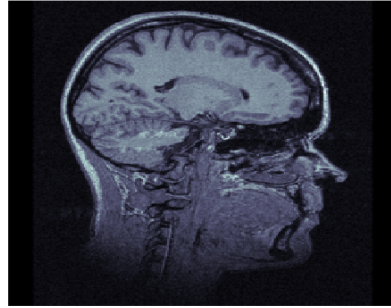


(d) Residual errors per outer iteration

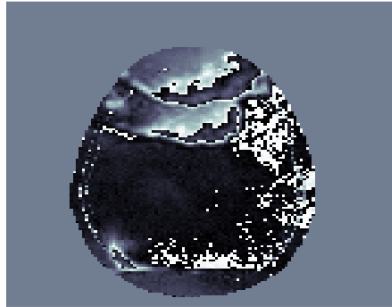
**Figure 4:** Errors during reconstruction of phantom. In the first two rows, errors are recorded for each application of  $A$ . We note that hybrid methods attain roughly the same numerical accuracy as framelet based methods. However, visual inspection of fig. 3d suggests that methods penalizing total variation result in a higher quality image here. In fig. 4c and fig. 4d we see that the framelet term allows us to execute more outer iterations before the iteration limit is reached.



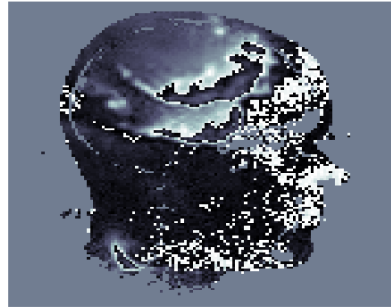
(a) 128x128 clean axial MRI



(b) 256x256 noisy sagittal MRI

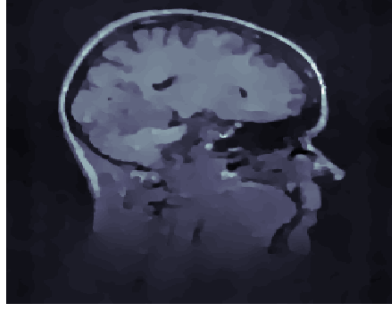


(c) Field map used with fig. 5a, values range from  $-15$  to  $15$  Hz.

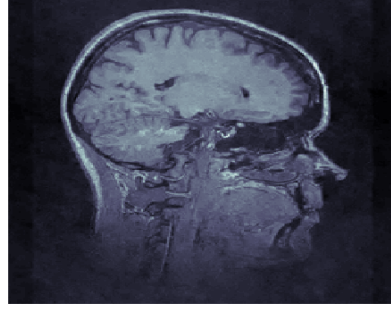


(d) Field map used with fig. 5b, values range from  $-15$  to  $15$  Hz.

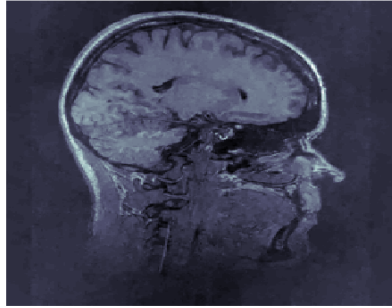
**Figure 5:** Exact images and field maps used in experiments.



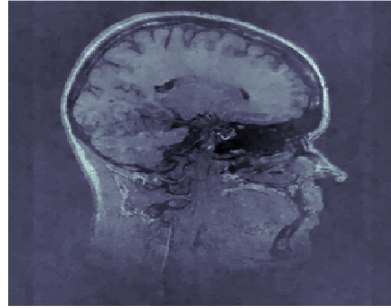
(a) TV



(b) Framelet

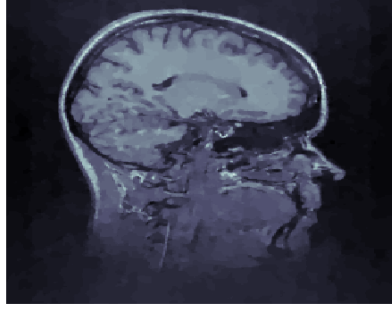


(c) Hybrid,  $\nu = 1$

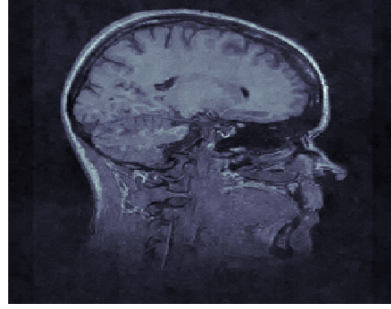


(d) Hybrid,  $\nu = .01$

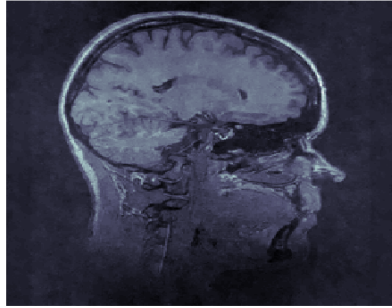
**Figure 6:** Comparison of image reconstructions from 40% data. All experiments were stopped after 3000 applications of  $A$ . Average computation time was 535.69 seconds. Total variation has removed noise but has blurred important features. The framelet based regularization in fig. 6b produced the highest quality image here.



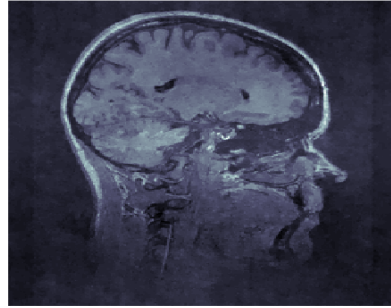
(a) TV



(b) Framelet



(c) Hybrid,  $\nu = 1$



(d) Hybrid,  $\nu = .01$

**Figure 7:** Comparison of image reconstructions from 40% data. All experiments were stopped after 10000 applications of  $A$ . Average computation time was 1767.2 seconds. Total variation has had time to produce a more detailed image than in fig. 6a. The regularizations involving framelets have produced similar images.



For two-dimensional datasets, we used a Shepp-Logan phantom (cf. fig. 2 and fig. 5a) and the standard Matlab MRI data set as our clean images. To validate our method on realistic and noisy data, we obtained a sagittal MRI of the head courtesy of Dr. Rohan Dharmakumar from Mount Sinai Hospital (cf. fig. 5).

For our three-dimensional dataset we used a T1-weighted volume scan of a healthy 22 year old male taken on a Bruker BioSpin at 4.3T with 128x128x128 resolution obtained from the LONI Image Database at <https://ida.loni.ucla.edu> (cf. fig. 9). We retrospectively undersampled  $k$ -space uniformly down to 40% before our volume reconstruction experiment. For the hybrid regularization in three dimensions, we used a Haar wavelet term. While it is known that Haar wavelets are suboptimal for MRI reconstruction [20], a three dimensional framelet library is not yet available. Even with a suboptimal regularization, the additional term speeds computation enough that a Hybrid regularization still outperforms the total variation regularization, fig. 10.

Model field maps were obtained by scaling a smoothed and noisy image to values comparable with empirically observed maps [2]. In practice, the complete field map is often unattainable and one must estimate it from multiple scans [67]. For each experiment, two acquisitions at echo times differing by  $\Delta_1 = 2\text{msec}$  were simulated to produce images:

$$y_1 = \rho + \sigma_1 \quad (40)$$

$$y_2 = e^{iz(\mathbf{x})\Delta_1} \rho + \sigma_2 \quad (41)$$

allowing us to obtain an estimate for the field map:

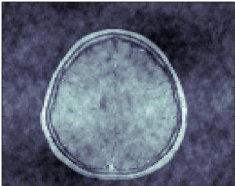
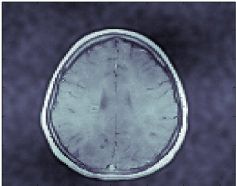
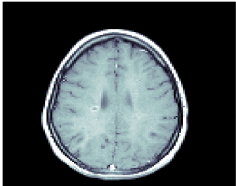
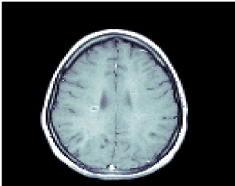
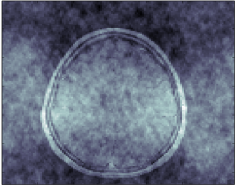
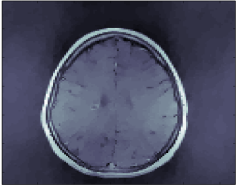
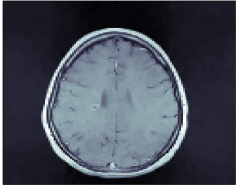
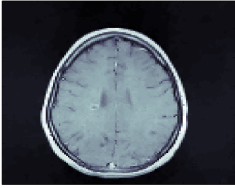
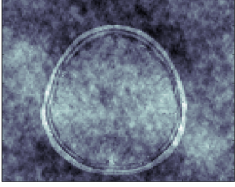

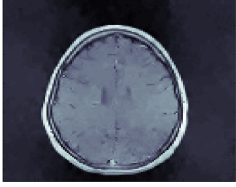
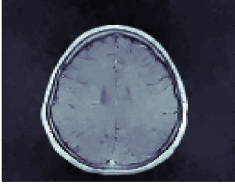
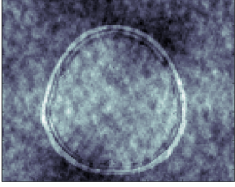



$$z(\mathbf{x}) = \text{Arg}(y_1^* y_2) / \Delta_1 \quad (42)$$

For all imaging experiments the same background field was used, the estimate, however, was re-computed for each image. In our volume reconstruction experiment we stacked the background field image along the  $z$ -axis and repeated the procedure in eq. (42).

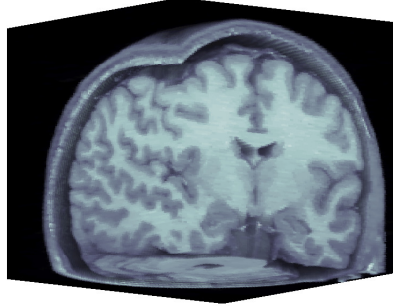
Plotting errors per iteration in fig. 4c and fig. 4d we see that total variation is the most efficient per outer loop iteration. This suggests that total variation alone may be advisable when the  $\rho^{k+1}$  update can be done analytically. However, when the number of matrix multiplications is taken into account, total variation is outperformed by other regularization strategies (cf. fig. 8 and fig. 3). When the data contains noise reconstruction is more difficult (cf. fig. 6 and fig. 7).

## 4 Conclusion

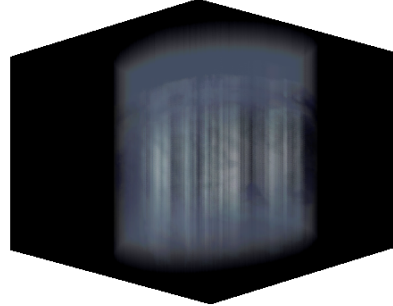
We have presented an efficient and fast-converging algorithm for MRI image reconstruction in the presence of inhomogeneous fields. This requires knowledge of the  $k$ -space trajectory and field inhomogeneity profile. The latter could be obtained in real time using  $B_0$  mapping techniques. The former is prescribed by the imaging pulse sequence. The technique should be applicable to the class of problems where the signal is a linear function of the spin density,  $s = A\rho$ , and the matrix  $A$  can be decomposed into inhomogeneity and spatial encoding matrices. We note that the case of low-field MRI, the signal equation (3) is also of the form  $s = A\rho$ , where  $A$  can be separated into encoding and inhomogeneity matrices. One difference is that computational overhead is increased due to the requirement for computing products of non-commutative rotation matrices. A more important difference is that the encoding matrix is no longer of type NUFFT. It is unclear at this stage if such non-NUFFT matrices would lead to convergence of our algorithm. Further investigations would be needed.

NUFFT	TV	Framelet	Hybrid, $\nu = 1$
			
			
			
			

**Figure 8:** Clean brain image reconstruction. Rows correspond to downsample factors of 66%, 40%, 29% and 22%. All iterative methods were stopped after 3000 applications of  $A$ . Average reconstruction time was 147.83 seconds.

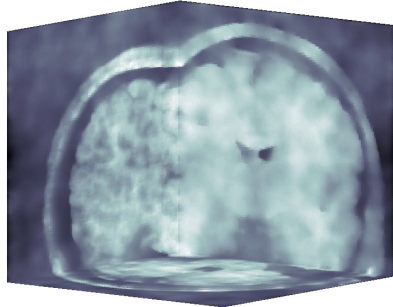


(a) Exact

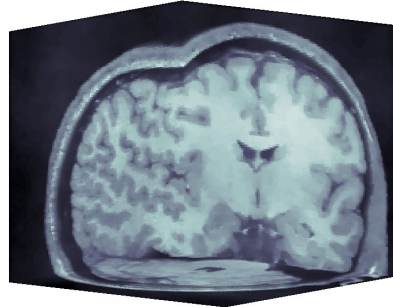


(b) Field map, values range from  $-15$  to  $15$  Hz.

**Figure 9:** Exact data used in volume reconstruction experiment. The volume dataset size was  $128 \times 128 \times 128$ . Field map values range from  $-15$  to  $15$  Hz, alpha mapping in fig. 9b has been reduced to make the most distorted parts of the volume visible.



(a) TV



(b) Hybrid,  $\nu = 1$

**Figure 10:** Volume reconstruction of a brain scan at 40% undersampling. All iterative methods are stopped after 5500 applications of  $A$ . Average computation time was 2981.13 seconds. The average number of applications of  $A$  required to update  $\rho^{k+1}$  was 124.22 when a total variation regularizer was used. This was reduced to 9.79 with the hybrid method.

## References

- [1] M. Lustig, D. Donoho, and J. Pauly, "Sparse MRI: The application of compressed sensing for rapid MR imaging.," *Magnetic resonance in medicine*, vol. 58, pp. 1182–1195, Dec. 2007.
- [2] J. Fessler, V. Olafsson, H. Shi, and D. Noll, "Toeplitz-based iterative image reconstruction for MRI with correction for magnetic field inhomogeneity," *IEEE Transactions on Signal Processing*, vol. 53, pp. 3393–3402, Sept. 2005.
- [3] P. Mansfield, *NMR Imaging in Biomedicine (Advances in magnetic resonance)*. Academic Press, 1982.
- [4] P. J. Prado, "Single sided imaging sensor," *Magnetic Resonance Imaging*, vol. 21, pp. 397–400, Apr. 2003.
- [5] J. Perlo, "3D imaging with a single-sided sensor: an open tomograph," *Journal of Magnetic Resonance*, vol. 166, pp. 228–235, Feb. 2004.
- [6] J. Paulsen, J. Franck, V. Demas, and L.-S. Bouchard, "Least squares magnetic-field optimization for portable nuclear magnetic resonance magnet design," *IEEE Transactions on*, vol. 44, no. 12, pp. 4582–4590, 2008.
- [7] B. Blumich, P. Blumer, G. Eidman, A. Guthausen, R. Haken, U. Schmitz, K. Saito, and G. Zimmer, "The NMR-Mouse: Construction, Excitation, and Applications," *Magnetic resonance imaging*, vol. 16, pp. 479–484, Jan. 1998.
- [8] A. E. Marble, I. V. Mastikhin, B. G. Colpitts, and B. J. Balcom, "A constant gradient unilateral magnet for near-surface MRI profiling.," *Journal of magnetic resonance (San Diego, Calif. : 1997)*, vol. 183, pp. 228–34, Dec. 2006.
- [9] J. M. Franck, V. Demas, R. W. Martin, L.-S. Bouchard, and A. Pines, "Shimmed matching pulses: simultaneous control of rf and static gradients for inhomogeneity correction.," *The Journal of chemical physics*, vol. 131, p. 234506, Dec. 2009.
- [10] D. Topgaard, R. W. Martin, D. Sakellariou, C. A. Meriles, and A. Pines, "'Shim pulses" for NMR spectroscopy and imaging.," *Proceedings of the National Academy of Sciences of the United States of America*, vol. 101, pp. 17576–81, Dec. 2004.
- [11] C. A. Meriles, D. Sakellariou, H. Heise, and A. Pines, "Approach to High-Resolution ex Situ NMR Spectroscopy," *Science*, vol. 293, no. July, pp. 82–85, 2001.
- [12] C. a. Meriles, D. Sakellariou, A. H. Trabesinger, V. Demas, and A. Pines, "Zero- to low-field MRI with averaging of concomitant gradient fields.," *Proceedings of the National Academy of Sciences of the United States of America*, vol. 102, pp. 1840–2, Feb. 2005.
- [13] N. Kelso, S.-K. Lee, L.-S. Bouchard, V. Demas, M. Mück, A. Pines, and J. Clarke, "Distortion-free magnetic resonance imaging in the zero-field limit.," *Journal of magnetic resonance (San Diego, Calif. : 1997)*, vol. 200, pp. 285–90, Oct. 2009.
- [14] L.-S. Bouchard, "Unidirectional magnetic-field gradients and geometric-phase errors during Fourier encoding using orthogonal ac fields," *Physical Review B*, vol. 74, pp. 1–11, Aug. 2006.
- [15] L.-S. Bouchard and M. Anwar, "Synthesis of matched magnetic fields for controlled spin precession," *Physical Review B*, vol. 76, pp. 1–10, July 2007.
- [16] E. M. Haacke and R. Brown, "Magnetic Resonance Imaging Physical Principles and Sequence Design," 1999.
- [17] J. Romberg, "Imaging via Compressive Sampling," *IEEE Signal Processing Magazine*, no. March 2008, pp. 14–20, 2007.
- [18] M. Guerquin-Kern, M. Häberlin, K. P. Pruessmann, and M. Unser, "A fast wavelet-based reconstruction method for magnetic resonance imaging.," *IEEE transactions on medical imaging*, vol. 30, pp. 1649–60, Sept. 2011.
- [19] J. Aelterman, H. Q. Luong, B. Goossens, A. Pižurica, and W. Philips, "Augmented Lagrangian based reconstruction of non-uniformly sub-Nyquist sampled MRI data," *Signal Processing*, vol. 91, pp. 2731–2742, Dec. 2011.
- [20] L. Chaâri, J.-C. Pesquet, A. Benazza-Benyahia, and P. Ciuciu, "A wavelet-based regularized reconstruction algorithm for SENSE parallel MRI with applications to neuroimaging.," *Medical image analysis*, vol. 15, pp. 185–201, Apr. 2011.
- [21] Q. Yang, M. Smith, and J. Wang, "Magnetic susceptibility effects in high field MRI," *Biological Magnetic Resonance*, vol. 26, pp. 249–284, 2006.
- [22] T.-k. Truong, D. W. Chakeres, and P. Schmalbrock, "Effects of B 0 and B 1 Inhomogeneity in Ultra-High Field MRI," *Proc. Intl. Soc. Mag. Reson. Med.*, vol. 11, p. 2170, 2004.

- [23] J. Reichenbach, R. Venkatesan, D. Yablonskiy, M. R. Thompson, and E. M. Haacke, "Theory and Application of Static Field Inhomogeneity Effects in Gradient- Echo Imaging," *Journal of Magnetic Resonance Imaging*, vol. 7, pp. 266–279, 1997.
- [24] M. a. Moerland, R. Beersma, R. Bhagwandien, H. K. Wijrdeman, and C. J. Bakker, "Analysis and correction of geometric distortions in 1.5 T magnetic resonance images for use in radiotherapy treatment planning.," *Physics in medicine and biology*, vol. 40, pp. 1651–1654, Oct. 1995.
- [25] A. Neufeld, Y. Assaf, M. Graif, T. Hendler, and G. Navon, "Susceptibility-matched envelope for the correction of EPI artifacts.," *Magnetic resonance imaging*, vol. 23, pp. 947–951, Nov. 2005.
- [26] R. C. McKinstry and D. Y. Jarrett, "Magnetic Susceptibility Artifacts on MRI: A Hairy Situation," *American Journal of Roentgenology*, vol. 182, no. February, pp. 532–535, 2004.
- [27] I. C. Duncan, "The "Aura" Sign: An Unusual Cultural Variant Affecting MR Imaging," *American Journal of Roentgenology*, no. December, pp. 1485–1489, 2001.
- [28] F. Baselice, G. Ferraioli, and A. Shabou, "Field map reconstruction in magnetic resonance imaging using Bayesian estimation.," *Sensors*, vol. 10, pp. 266–79, Jan. 2010.
- [29] Kressler B, T. Liu, P. Spincemaille, Q. Jiang, and Y. Wang, "Nonlinear regularization for per voxel estimation of magnetic susceptibility distributions from MRI field maps.," *IEEE transactions on medical imaging*, vol. 29, pp. 273–281, Feb. 2010.
- [30] J. A. Fessler, S. Member, and B. P. Sutton, "Nonuniform Fast Fourier Transforms Using Min-Max Interpolation," vol. 51, no. 2, pp. 560–574, 2003.
- [31] J. Fessler, "Model-Based Image reconstruction for MRI," *IEEE Signal Processing Magazine*, vol. 936726, no. July, pp. 81–89, 2010.
- [32] B. P. Sutton, S. Member, D. C. Noll, J. A. Fessler, and S. Member, "Fast , Iterative Image Reconstruction for MRI in the Presence of Field Inhomogeneities," *IEEE transactions on medical imaging*, vol. 22, no. 2, pp. 178–188, 2003.
- [33] K. T. Block, M. Uecker, and J. Frahm, "Undersampled radial MRI with multiple coils. Iterative image reconstruction using a total variation constraint.," *Magnetic resonance in medicine*, vol. 57, pp. 1086–98, June 2007.
- [34] S. Ramani and J. A. Fessler, "An Accelerated Iterative Reweighted Least Squares Algorithm for Compressed Sensing MRI," *IEEE ISBI*, pp. 257–260, 2010.
- [35] B. J. Wilm, C. Barmet, M. Pavan, and K. P. Pruessmann, "Higher order reconstruction for MRI in the presence of spatiotemporal field perturbations.," *Magnetic resonance in medicine*, vol. 1701, pp. 1690–1701, Apr. 2011.
- [36] W. Chen, C. T. Sica, and C. H. Meyer, "Fast conjugate phase image reconstruction based on a Chebyshev approximation to correct for B0 field inhomogeneity and concomitant gradients.," *Magnetic Resonance in Medicine*, vol. 60, pp. 1104–11, Nov. 2008.
- [37] H. Schomberg, "Off-resonance correction of MR images.," *IEEE transactions on medical imaging*, vol. 18, pp. 481–495, June 1999.
- [38] D. C. Noll, J. a. Fessler, and B. P. Sutton, "Conjugate phase MRI reconstruction with spatially variant sample density correction.," *IEEE Transactions on Medical Imaging*, vol. 24, pp. 325–36, Mar. 2005.
- [39] T. Goldstein and S. Osher, "The Split Bregman Method for L1-Regularized Problems," *SIAM Journal on Imaging Sciences*, vol. 2, no. 2, p. 323, 2009.
- [40] J. F. Cai, S. Osher, and Z. Shen, "Split Bregman Methods and Frame Based Image Restoration," *Multiscale Modeling & Simulation*, vol. 8, no. 2, p. 337, 2010.
- [41] J. Fessler, V. Olafsson, H. Shi, and D. Noll, "Toeplitz-based iterative image reconstruction for MRI with correction for magnetic field inhomogeneity," *IEEE Transactions on Signal Processing*, vol. 53, pp. 3393–3402, Sept. 2005.
- [42] L. Greengard and J.-Y. Lee, "Accelerating the Nonuniform Fast Fourier Transform," *SIAM Review*, vol. 46, no. 3, p. 443, 2004.
- [43] P. Irarrazabal, C. H. Meyer, D. G. Nishimura, and A. Macovski, "Inhomogeneity correction using an estimated linear field map.," *Magnetic resonance in medicine*, vol. 35, pp. 278–82, Feb. 1996.
- [44] L.-c. Man, J. M. Pauly, and A. Macovski, "Multifrequency Interpolation for Fast Off-resonance Correction," *Magnetic resonance in medicine*, pp. 785–792, 1996.

- [45] D. Noll, *Reconstruction Techniques for Magnetic Resonance Imaging*. PhD thesis, Stanford University, 1991.
- [46] H. Moriguchi, B. M. Dale, J. S. Lewin, and J. L. Duerk, "Block regional off-resonance correction (BRORC): a fast and effective deblurring method for spiral imaging.," *Magnetic resonance in medicine*, vol. 50, pp. 643–8, Sept. 2003.
- [47] V. Rokhlin, A. Szlam, and M. Tygert, "A randomized algorithm for PCA," *Siam J matrix anal. appl.*, vol. 31, no. 3, pp. 1100–1124, 2009.
- [48] P.-G. Martinsson, V. Rokhlin, and M. Tygert, "A randomized algorithm for the decomposition of matrices," *Applied and Computational Harmonic Analysis*, vol. 30, pp. 47–68, Jan. 2011.
- [49] N. Halko, P. Martinsson, and J. Tropp, "Finding structure with randomness: Probabilistic algorithms for constructing approximate matrix decompositions," *SIAM Review*, vol. 53, no. 2, pp. 217–288, 2011.
- [50] E. Liberty, F. Woolfe, P.-G. Martinsson, V. Rokhlin, and M. Tygert, "Randomized algorithms for the low-rank approximation of matrices.," *Proceedings of the National Academy of Sciences of the United States of America*, vol. 104, pp. 20167–72, Dec. 2007.
- [51] C. Papadimitriou, H. Tamaki, and P. Raghavan, "Latent semantic indexing: A probabilistic analysis," *Proceedings of the*, pp. 1–18, 1998.
- [52] A. Çivril and M. Magdon-Ismail, "On selecting a maximum volume sub-matrix of a matrix and related problems," *Theoretical Computer Science*, vol. 410, pp. 4801–4811, Nov. 2009.
- [53] G. Golub and C. V. Loan, *Matrix Computations*. Johns Hopkins University Press, 3rd ed., 1996.
- [54] M. Gu and S. C. Eisenstat, "An Efficient Algorithm for Computing a Strong Rank-Revealing QR Factorization," *SIAM Journal on Scientific Computing*, vol. 17, no. 4, pp. 848–869, 1996.
- [55] E. Candes, J. Romberg, and T. Tao, "Stable Signal Recovery from Incomplete and Inaccurate Measurements arXiv : math / 0503066v2 [ math . NA ] 7 Dec 2005," *Science*, vol. 40698, pp. 1–15, 2005.
- [56] E. Candes, J. Romberg, and T. Tao, "Robust uncertainty principles: exact signal reconstruction from highly incomplete frequency information," *IEEE Transactions on Information Theory*, vol. 52, pp. 489–509, Feb. 2006.
- [57] S. O. Jian-Feng Cai, Bin Dong and Z. Shen, "Image restoration: Total variation: Wavelet frams: and beyond, march 2011," *UCLA CAM reports*, 2011.
- [58] L. Rudin, S. Osher, and E. Fatemi, "Nonlinear total variation based noise removal algorithms," *Physica D: Nonlinear Phenomena*, vol. 60, pp. 259–268, Nov. 1992.
- [59] D. Liang, H. Wang, and L. Ying, "SENSE reconstruction with nonlocal TV regularization.," *IEEE Engineering in Medicine and Biology Society*, vol. 2009, pp. 1032–1035, Jan. 2009.
- [60] S. Osher, M. Burger, D. Goldfarb, J. Xu, and W. Yin, "An Iterative Regularization Method for Total Variation-Based Image Restoration," *Multiscale Modeling & Simulation*, vol. 4, no. 2, p. 460, 2005.
- [61] D. G. J. X. Stanley Osher, Martin Burger and W. Yin, "An iterative regularization method for total variation-based image restoration," *SIAM Multiscale Model. Simul.*, vol. 4, no. 2, 2005.
- [62] E. Esser, "Applications of lagrangian-based alternating direction methods and connections to split bregman," *UCLA CAM reports*, no. 31, 2009.
- [63] "On the global and linear convergence of the generalized alternating direction method of multipliers,"
- [64] Z.-Q. L. Mingyi Hong, "On the linear convergence of the alternating direction method of multipliers," *arXiv:1208.3922*.
- [65] H. A. v. d. V. A. van der Sluis, "The rate of convergence of conjugate gradients," *Numerische Mathematik*, vol. 48, no. 5, 1986.
- [66] M. Frigo and S. G. Johnson, "The Design and Implementation of {FFTW3}," *Proceedings of the IEEE*, vol. 93, no. 2, pp. 216–231, 2005.
- [67] A. K. Funai, J. a. Fessler, D. T. B. Yeo, V. T. Olafsson, and D. C. Noll, "Regularized field map estimation in MRI.," *IEEE transactions on medical imaging*, vol. 27, pp. 1484–94, Oct. 2008.